Keškić, T.; Jagličić, Z.; Pevec, A.; Čobeljić, B.; Radanović, D.; Gruden, M.; Turel, I.; Anđelković, K.; Brčeski, I.; Zlatar, M. Synthesis, X-Ray Structures and Magnetic Properties of Ni(II) Complexes of Heteroaromatic Hydrazone. Polyhedron 2020, 191, 114802. https://doi.org/10.1016/j.poly.2020.114802

Synthesis, X-ray structures and magnetic properties of Ni(II) complexes of heteroaromatic hydrazone

Tanja Keškić,[a] Zvonko Jagličić,[b] Andrej Pevec,[c] Božidar Čobeljić,[a] Dušanka Radanović,[d] Maja Gruden,[a] Iztok Turel,[c] Katarina Anđelković,[a] Ilija Brčeski[a,*] and Matija Zlatar[d,*]

[a]*University of Belgrade-Faculty of Chemistry, Studentski trg 12-16, 11000 Belgrade, Serbia*

[b]*Institute of Mathematics, Physics and Mechanics & Faculty of Civil and Geodetic Engineering, University of Ljubljana, Jadranska 19, Ljubljana, Slovenia*

[c]*Faculty of Chemistry and Chemical Technology, University of Ljubljana, Večna pot 113, 1000 Ljubljana, Slovenia*

[d]*University of Belgrade-Institute of Chemistry, Technology and Metallurgy, National Institute of the Republic of Serbia, Njegoševa 12, 11000 Belgrade, Serbia*

*Corresponding authors:

Ilija Brčeski: ibrceski@chem.bg.ac.rs

Matija Zlatar: matijaz@chem.bg.ac.rs; matija.zlatar@ihtm.bg.ac.rs

Abstract

Two binuclear double end-on azido bridged Ni(II) complexes, $[Ni_2\mathbf{L}_2(\mu\text{-}_{1,1}\text{-}N_3)_2(N_3)_2]\cdot 2H_2O$ **(1a),** and $[Ni_2\mathbf{L}_2(\mu\text{-}_{1,1}\text{-}N_3)_2(N_3)_2]\cdot 4H_2O$ **(1b)** having the same inner sphere, where **L**=((*E*)-*N*,*N*,*N*-trimethyl-2-oxo-2-(2-(1-(thiazol-2-yl)ethylidene)hydrazinyl)ethan-1-aminium, were synthesized from the same solution and characterized by single-crystal X-ray diffraction methods. Variable-temperature magnetic susceptibility measurements showed intra-dimer ferromagnetic coupling between Ni(II) ions. The ferromagnetic coupling is supported by the broken-symmetry DFT calculations, with the level of theory chosen based on a benchmark study on 19 additional structurally related binuclear Ni(II) complexes. The role of water molecules in crystals of **1a** and **1b** is explained by DFT based energy decomposition analysis.

Keywords:

Ni(II) binuclear complexes - X-ray structure - ferromagnetic coupling - broken symmetry DFT - double-hybrid functionals - Energy Decomposition Analysis

1.Introduction

The versatility of the coordination modes of the azide ion and its effectiveness to propagate the magnetic interaction between the paramagnetic centers made this ligand an attractive target for extensive studies [1–27]. The azide anion is a good bridging ligand for M(II) ions like Cu(II) [2–8,13,23], Ni(II) [1,2,9–23] and Mn(II) [1,2,23]. In general, it may give many bridging coordination modes, Scheme 1: single and double $\mu_{1,3}$-N_3 and $\mu_{1,1}$-N_3, $\mu_{1,1,3}$-N_3, $\mu_{1,1,1}$-N_3, $\mu_{1,1,1,1}$-N_3, $\mu_{1,1,3,3}$-N_3, and $\mu_{1,1,1,3,3,3}$-N_3 [1,13,23] of which two coordination modes end-to-end ($\mu_{1,3}$-N_3) and end-on ($\mu_{1,1}$-N_3) are the most common. Although complicated bonding modes of azide anion are rare, they have been observed in some Cu(II) and Ni(II) complexes [5–8,23]. Alternative $\mu_{1,3}$-N_3 and $\mu_{1,1}$-N_3 bridges were also found in several systems [1,24]. The diverse binding modes of the bridging azide anion can lead to the formation of metal complexes of interesting structures with different nuclearity and dimensionality. According to the dimensionality the azido-bridged complexes can be divided into discrete molecules [1,23,25], one-dimensional [1,3,5–8,24], two-dimensional [1,5–7] and three-dimensional [1,8] systems.

The bridging modes of the azide anion strongly influence the magnetic interactions between adjacent paramagnetic metal ions. When the azido group acts as bridging ligand with end-on coordination, the resulting binuclear complexes usually show ferromagnetic behavior. In contrast, when it is coordinated in an end-to-end fashion, antiferromagnetic coupling emerges. The angles within the M–$(N_3)_n$–M unit are the primary determinant of the type and magnitude of the exchange coupling [1,2]. The bond distances between the metal ion and bridging atoms also have a strong influence on the coupling constant, with the ferromagnetic coupling diminishing upon increasing such distances [2].

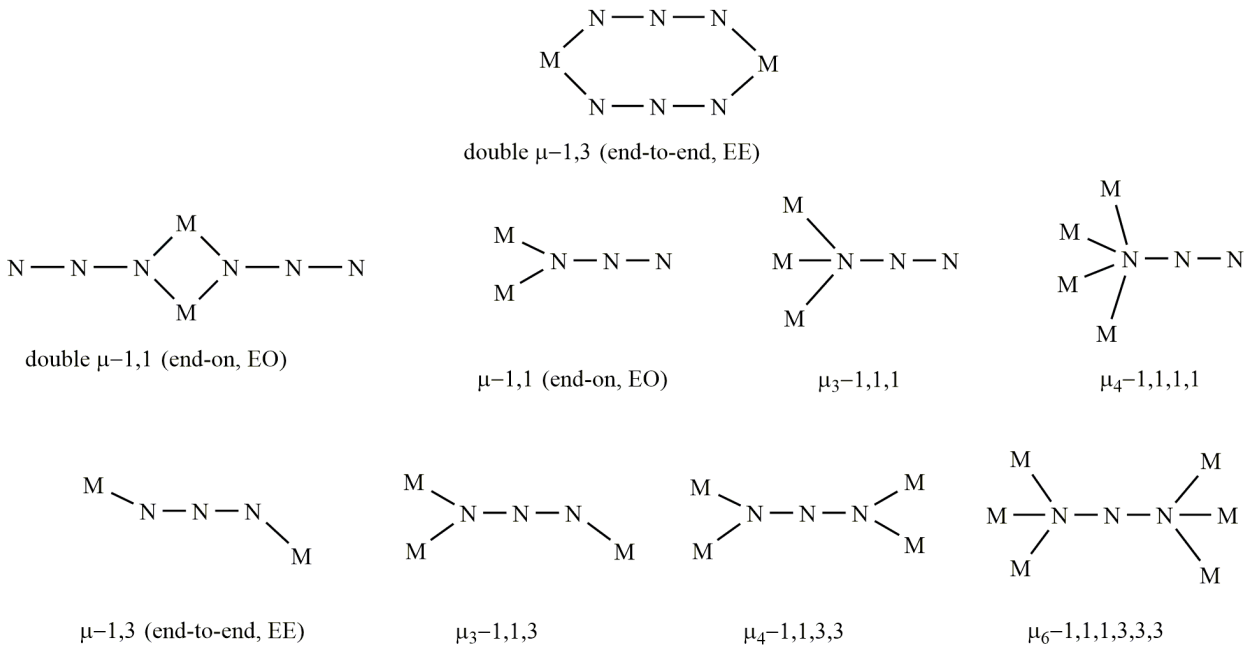

Scheme 1. Different azido bridging modes.

Recently, we have reported the structural and magnetic studies of double end-on azido-bridged binuclear complexes of Ni(II), Co(II) and Cu(II) with N-heteroaromatic monohydrazones of Girard's T reagent (trimethylammoniumacetohydrazide chloride), $[M_2(\mathbf{L^1})_2(\mu_{1,1}\text{-}N_3)_2(N_3)_2]\cdot H_2O\cdot CH_3OH$ (M = Ni(II), Co(II) [9,27], $\mathbf{L^1}$ = (*E*)-*N*,*N*,*N*-trimethyl-2-oxo-2-(2-(quinolin-2-ylmethylene)hydrazinyl)ethan-1-aminium), and $[Cu_2(\mathbf{L^2})_2(\mu_{1,1}\text{-}N_3)_2](ClO_4)_2$ [4] ($\mathbf{L^2}$ = (*E*)-*N*,*N*,*N*-trimethyl-2-oxo-2-(2-(1-(pyridin-2-yl)ethylidene)hydrazinyl)ethan-1-aminium)), in which the metallic centers are ferromagnetically coupled. As a continuation of our study on double end-on azido-bridged binuclear complexes of M(II) ions with heteroaromatic monohydrazones of Girard's T reagent, in this paper, we report the synthesis, crystal structure and magnetic property of double end-on binuclear Ni(II) complex, $[Ni_2\mathbf{L}_2(\mu\text{-}_{1,1}\text{-}N_3)_2(N_3)_2]$ (**1**) (**L**–(*E*)-*N*,*N*,*N*-trimethyl-2-oxo-2-(2-(1-(thiazol-2-yl)ethylidene)hydrazinyl)ethan-1-aminium). The complex **1** crystallized as dihydrate (**1a**) and tetrahydrate (**1b**). The crystals of both complexes have been subjected to the X-ray structure analysis.

In parallel, a computational study based on the broken-symmetry density functional theory (BS-DFT) [28–32] has been carried out. The BS-DFT is a well-known procedure for studying exchange-coupled transition metal complexes [32–37]. In BS-DFT, the exchange coupling

constant (*J*) is related to the energy differences between the electronic states with different spin multiplicity. Albeit, the accuracy of such calculations is very sensitive to the applied density functional approximation (DFA) [38–42]. Additionally, the suitability of DFAs for magnetic exchange is limited to a small chemical space, i.e., the optimal choice of DFA is often constrained to a specific type of chemical system. The standard benchmark set for appraisal of the influence of DFAs on calculated *J* consists of a small set of Cu(II) dimers [40-43]. Recently, the performance of double-hybrid functionals were studied on a set of five challenging binuclear manganese [39]. For binuclear end-on azido bridged Ni(II) complexes, computational studies are scarce [1, 2, 9]. Therefore, herein we assessed the quality of various DFAs for the calculation of *J* in end-on azido bridged binuclear Ni(II) complexes. For this purpose, 14 DFAs with different flavors were selected (general gradient approximations (GGAs), meta-GGAs, hybrid functionals, meta-hybrid functionals, and double-hybrid functionals). These 14 exchange-correlation functionals were used for the calculations of *J* constants in 19 structurally related binuclear Ni(II) complex, for which the *J* value was determined experimentally. Based on this assessment, three DFAs were chosen for the calculation of *J* constant in **1a** and **1b**. The magnetic coupling is rationalized from the structural parameters and considering the electronic structure of complexes and the delocalization of the spin-density from DFT calculations. Moreover, the role of lattice water molecules in crystals of **1a** and **1b** is explained by DFT based energy decomposition analysis [44–46] coupled with natural orbitals for chemical valence scheme (EDA-NOCV) [47,48].

2. Experimental

2.1. Materials and methods

2-Acetylthiazole (99%) and Girard's T reagent (99%) were obtained from Sigma-Aldrich. IR spectra were recorded on a Nicolet 6700 FT-IR spectrometer using the ATR technique in the region 4000−400 cm^{-1} (vs-very strong, s-strong, m-medium, w-weak, bs - broad signal). ^{1}H and ^{13}C NMR spectra were recorded on Bruker Avance 500 spectrometer (^{1}H at 500 MHz; ^{13}C at 125 MHz) at room temperature using TMS as the internal standard in DMSO-d^6 (numbering of atoms according to the Scheme 2). Chemical shifts are expressed in ppm (δ) values and coupling constants (*J*) in Hz. Elemental analyses (C, H, N, and S) were performed by standard micro-methods using the ELEMENTARVario ELIII C.H.N.S.O analyzer.

*2.1.1. Synthesis of (E)-N,N,N-trimethyl-2-oxo-2-(2-(1-(thiazol-2-yl)ethylidene)hydrazinyl)ethan-1-aminium chloride (**HL**Cl)*

The ligand **HL**Cl was synthesized by the reaction of Girard's reagent T (1.676 g, 10 mmol) and 2-acetylthiazole (1036 μL, 10 mmol) in water (20 ml). The reaction mixture was acidified with 3-4 drops of 2 M HCl and refluxed for 3 h. After cooling to the room temperature, white precipitate was filtered and washed with water. Yield: 2.539 g (92 %). Elemental analysis calcd. for $C_{10}H_{17}N_4OSCl$: C 43.40 %, H 6.19 %, N 20.24 %, S 11.58 %; found: C 43.45 %, H 6.21 %, N 20.20 %, S 11.52 %. IR (ATR, cm^{-1}): 3387.1 (w), 3128.6 (w), 3091.8 (m), 3017.9 (m), 2955.5 (s), 1701.7 (vs), 1612.5 (w), 1550.0 (vs), 1486.8 (s), 1401.4 (m), 1300.4 (w), 1201.4 (s), 1135.3 (w), 976.2 (w), 944.7 (w), 914.3 (m), 786.9 (w), 748.5 (w), 684.0 (w), 585.1 (w), 551.7 (w). ^{1}H NMR (500 MHz, DMSO-d^6), δ (ppm): 2.41 (s, 3H, C5-H), 2.53 (s, 3H, C5-H), 3.30 (s, 9H, C8-H), 3.34 (s, 9H, C8-H), 4.60 (s, 2H, C7-H), 4.82 (s, 2H, C7-H), 7.848 (d, 1H, $J_{C2\text{-}H/C3\text{-}H}$ = 5 Hz, C2-H), 7.854 (d, 1H, $J_{C2\text{-}H/C3\text{-}H}$ = 5 Hz, C2-H), 7.926 (d, 1H, $J_{C2\text{-}H/C3\text{-}H}$ = 5 Hz, C3-H), 7.932 (d, 1H, $J_{C2\text{-}H/C3\text{-}H}$ = 5 Hz, C3-H), 11.61 (s, 1H, N-H), 11.86 (s, 1H, N-H). ^{13}C NMR (125 MHz, DMSO-d^6), δ (ppm): 13.90 (C5), 15.05 (C5), 53.65 (C8), 53.89 (C8), 63.01 (C7), 63.76 (C7), 123.33 (C2), 123.65 (C2), 143.94 (C3), 143.97 (C3), 146.98 (C4), 150.80 (C4), 161.23 (C1), 166.78 (C1), 167.04 (C6), 167.34 (C6).

*2.1.2. Synthesis of $[Ni_2\mathbf{L}_2(\mu\text{-}_{1,1}\text{-}N_3)_2(N_3)_2]\cdot 2H_2O$ (**1a**) and $[Ni_2\mathbf{L}_2(\mu\text{-}_{1,1}\text{-}N_3)_2(N_3)_2]\cdot 4H_2O$ (**1b**) complexes*

The complex **1** was synthesized by the reaction of ligand **HL**Cl (83 mg, 0.30 mmol) (15/15 mL), $NiCl_2\cdot 6H_2O$ (72 mg, 0.30 mmol) and NaN_3 (80 mg, 1.2 mmol) in the mixture of methanol/acetonitrile (15/15 mL). First the ligand was dissolved, after which solid Ni(II) and N_3^- salts were added. The reaction mixture was stirred for three hours at 65 °C. After refrigeration of the solution at –7°C for ten days, two types of yellow crystals suitable for X-ray analysis were formed. Elemental analysis calcd. for $C_{20}H_{40}N_{20}Ni_2O_6S_2$: C 28.66 %, H 4.81 %, N 33.42 %, S 7.65 %; found: C 28.45 %, H 4.85 %, N 33.27 %, S 7.61 %. IR (ATR, cm^{-1}): 3394.9 (m), 3096.3 (w), 2957.8 (w), 2146.6 (m), 2053.7 (vs), 2034.2 (vs), 1602.6 (w), 1531.9 (s), 1479.4 (m), 1404.1 (m), 1248.3 (m), 1154.9 (w), 1052.3 (w), 1011.8 (m), 975.2 (w), 913.3 (w), 888.3 (w), 783.3 (w), 736.3 (w), 640.8 (w).

2.2. X-ray Crystallography

Crystal data and refinement parameters of compounds **1a** and **1b** are listed in Table 1. X-ray intensity data were collected at 150 K for **1a** and at room temperature for **1b** with Agilent SuperNova dual-source diffractometer with an Atlas detector equipped with mirror-monochromated Mo Kα radiation (λ = 0.71073 Å). The data were processed using CRYSALIS PRO [49]. The structures were solved by direct methods (SIR-92 [50]) and refined by a full-matrix least-squares procedure based on F^2 using SHELXL-2014 [51]. All non-hydrogen atoms were refined anisotropically. The water hydrogen atoms were located in a difference map and refined with the distance restraints (DFIX) with O–H = 0.96 Å and with U_{iso}(H) = 1.5U_{eq}(O). All other hydrogen atoms were included in the model at geometrically calculated positions and refined using a riding model.

Table 1. Crystal data and structure refinement details for **1a** and **1b**.

	1a	**1b**
formula	$C_{20}H_{36}N_{20}Ni_2O_4S_2$	$C_{20}H_{40}N_{20}Ni_2O_6S_2$
Fw (g mol^{-1})	802.23	838.26
crystal size (mm)	0.10 × 0.10 × 0.05	0.70 × 0.20 × 0.10
crystal color	yellow	yellow
crystal system	triclinic	monoclinic
space group	*P* –1	*P* $2_1/c$
a (Å)	8.7014(8)	13.2446(7)
b (Å)	9.9706(9)	11.0402(6)
c (Å)	11.1502(10)	12.3962(6)
α (º)	65.851(8)	90.00
β (º)	81.231(8)	99.765(5)
γ (º)	68.810(9)	90.00
V (Å^3)	823.02(15)	1786.35(16)
Z	1	2

calcd density (g cm^{-3})	1.619	1.558
F(000)	416	872
no. of collected reflns	7762	10317
no. of independent reflns	4267	4092
R_{int}	0.0626	0.0290
no. of reflns observed	3433	3255
no. parameters	230	242
$R[I > 2\sigma(I)]^a$	0.0582	0.0344
wR_2(all data)^b	0.1577	0.0887
Goof , S^c	1.066	1.050
maximum/minimum residual electron density (e $Å^{-3}$)	+1.42/–0.85	+0.31/–0.35

$^aR = \sum||F_o| - |F_c||/\sum|F_o|$; $^bwR_2 = \{\sum[w(F_o^2 - F_c^2)^2]/\sum[w(F_o^2)^2]\}^{1/2}$; $^cS = \{\sum[w(F_o^2 - F_c^2)^2]/(n/p)\}^{1/2}$ where n is the number of reflections and p is the total number of parameters refined.

2.3. Magnetic Properties

Magnetic properties were investigated between 2 K and 300 K in a constant magnetic field of 1 kOe on a polynuclear sample using a Quantum Design MPMS-XL-5 SQUID magnetometer. The experimental results were corrected for the sample holder contribution and for a temperature-independent contribution of core electrons as obtained from Pascall's tables [52]. The molecular weight of **1b** has been used to calculate the molar susceptibility and to calculate the diamagnetic correction.

2.4. Computational details

The exchange coupling constant J of the Heisenberg-Dirac-van Vleck spin-Hamiltonian ($H = -2JS_1S_2$) was calculated with broken symmetry DFT formalism [28–32] according to the Yamaguchi approach [53] with the ORCA program package (version 4.1.2) [54]:

$$J = -\frac{E_{HS} - E_{BS}}{< S^2 >_{HS} - < S^2 >_{BS}}$$

$E_{HS} - E_{BS}$ is the calculated energy difference between the high-spin (quintet) and broken-symmetry states, and $< S^2 >_{HS}$ and $< S^2 >_{BS}$ are the corresponding spin expectation values. Scalar relativistic effects were considered at the Zero-Order-Regular-Approximation (ZORA) level [55]. ZORA-def2-TZVP(-f) [56,57] basis set for all atoms have been used. The assessment of DFAs on the calculated *J* values is performed on the set of ferromagnetically coupled binuclear tetraazido Ni(II) complexes with tridentate and bis-tridentate ligands (complexes **I**–**XVII** in Table S1, Supporting information (SI)). Additionally, binuclear double end-on azido Ni(II) complexes with tetradentate ligand (complexes **XVIII** and **XIX**) are included in the set. The last two complexes have the same inner sphere. However, **XVIII** shows weak antiferromagnetic coupling [58], while coupling in **XIX** is ferromagnetic [58], similarly to the other complexes **I–XVII**. The choice of DFAs include 14 functionals encompassing: GGAs (in the form of BP86 [59–61], BLYP [59,62–64], OLYP [62–65], OPBE [66]), meta-GGAs (M06-L [67,68], TPSS [69,70]), hybrid functionals (B3LYP [71], B3LYP* [72], BHandHLYP), meta-hybrid functionals (M06 [67,68], M06-2X [67,68], TPSSh [69,70]), and double-hybrid functionals (B2PLYP [73], PWPB95 [74]). The chain-of-spheres approximation to the exact exchange (COSX) [75] was employed. The scalar relativistically recontracted SARC/J [57,76,77] auxiliary basis sets have been used for the fitting of the Coulomb integrals in the resolution of the identity (RI) approximation [78]. The RI approach was used in the MP2 part of the calculation for double-hybrid functionals, in combination with def2-TZVP/C [79] correlation fitting basis sets. For GGA and meta-GGA functionals, RI approximation in the Split-RI-J variant was used. PWPB95, (double-hybrid with spin-opposite-spin MP2 approach), B2PLYP (standard double hybrid), and M06-2X (meta-hybrid) showed the best performance and were chosen for the calculation of *J* constant in complexes **1a** and **1b**. All the calculations were performed on the complexes from the experimentally determined X-ray structures: **1a** (CCDC 2009327), **1b** (CCDC 2009328), **I** (CCDC 1524733) [9], **II** (CCDC 272898) [10], **III** (CCDC 246819) [10], **IV** (CCDC 263466) [11], **V** (CCDC 709101) [12], **VI** (CCDC 907100) [13], **VII** (CCDC 1227541) [14], **VIII** (CCDC 119104) [15], **IX** (CCDC 1305130) [16], **X** (CCDC 895759) [17], **XI** (CCDC 917544) [17], **XII** (CCDC 705026) [18], **XIII** (CCDC 1477551) [19], **XIV** (CCDC 1562185) [20], **XV** (CCDC 1918387) [80], **XVI** (CCDC 172396) [21], **XVII** (CCDC 258211) [22], **XVIII** (CCDC 606336) [58], and **XIX** (CCDC 606335) [58].

Solvent molecules were removed, and hydrogen atoms were added where needed. Positions of hydrogen atoms were optimized, assuming the high-spin state, employing BP86 functional with Grimme's third-generation dispersion energy correction [81] and Becke-Johnson damping [82], i.e., BP86-D3. Positions of all other nuclei were fixed. When the two complexes were present in the unit cell (**III**, **IV**, **XIII**), the average of the two calculated *J* values is compared with the experiment. To compare all the results, reported *J* values, in those cases where the Hamiltonian in the form $H = -JS_1S_2$ is used (**III**, **VI**, **XII**), are divided by two.

To understand why **1b** is dominantly obtained, calculations on the model systems constructed from X-ray structures of **1a** and **1b** have been performed. The most straightforward models are bare, $[Ni_2\mathbf{L}_2(\mu\text{-}_{1,1}\text{-}N_3)_2(N_3)_2]$ structures, differing in geometries of binuclear units. The largest systems are dimers of binuclear units with a corresponding number of crystal H_2O molecules present. Positions of hydrogen atoms were optimized at BP86-D3/ZORA-def2-TZVP(-f) level of theory in dimeric structures of **1a** and **1b**, while heavy atoms are kept in their places determined by X-ray diffraction. Energies of model systems are evaluated at BP86-D3/ZORA-def2-TZVP(-f), B3LYP-D3/ZORA-def2-TZVP(-f) and M06-2X/ZORA-def2-TZVP(-f) level of theory. Energies of structures build from **1a** are supplemented with energies of optimized H_2O molecules at the same level of theory. The number of added H_2O molecules is chosen so that the pair of models have the same number of atoms. Therefore, it is possible to compare the stability of model systems based on **1a** and **1b**.

Geometry optimization of $[Ni_2\mathbf{L}_2(\mu\text{-}_{1,1}\text{-}N_3)_2(N_3)_2]$ starting from X-ray structures of **1a** and **1b** have been performed at ZORA-BP86-D4/TZP level of theory, with ADF program package (version 2019.302) [83–85], leading to two distinct conformations of the binuclear complex. Analytical harmonic frequencies [86,87] and IR intensities were calculated for both **1a** and **1b**. These calculations further ascertained that optimized structures are minima on the potential energy surfaces.

The role of lattice H_2O molecules in mediating the formation of supramolecular structures in the crystals of **1a** and **1b** was elucidated with the extended transition state energy decomposition analysis (EDA) [44-46] scheme as implemented in ADF program package at ZORA-BP86-D4/TZP level of theory. The interaction energy, E_{int}, between chosen fragments is decomposed into several chemically meaningful terms: (i) the quasi-classical electrostatic interaction between

the fragments (E_{elst}); (ii) the repulsive Pauli interaction (E_{Pauli}); and (iii) the stabilizing orbital interaction (E_{orb}); iv) dispersion correction (E_{disp}) because Grimme's dispersion energy correction (D4) is included. E_{orb} is further decomposed with the method of natural orbitals for chemical valence (NOCV), [47,48] to elucidate the importance of the covalency and polarization.

3. Results and discussion

3.1. Synthesis

The ligand (*E*)-*N*,*N*,*N*-trimethyl-2-oxo-2-(2-(1-(thiazol-2-yl)ethylidene)hydrazinyl)ethan-1-aminium chloride (**HL**Cl), was obtained by the condensation reaction of 2-acetylthiazole and Girard's T reagent, Scheme 2a. In the reaction of **HL**Cl with $NiCl_2 \cdot 6H_2O$ and NaN_3 in the molar ratio 1 : 1 : 3 in methanol/acetonitrile mixture of solvents, a binuclear double end-on azido bridged Ni(II) complex (**1b**), with composition $[Ni_2\mathbf{L}_2(\mu\text{-}_{1,1}\text{-}N_3)_2(N_3)_2]\cdot 4H_2O$ was obtained, Scheme 2b. Together with complex **1b**, in the same solution Ni(II) complex with composition $[Ni_2\mathbf{L}_2(\mu\text{-}_{1,1}\text{-}N_3)_2(N_3)_2]\cdot 2H_2O$ (**1a**) was formed in traces (few crystals were found visually). Changing solvents (water, methanol, ethanol, acetonitrile, mixtures of water/ethanol, water/acetonitrile, water/methanol/acetonitrile in different volume ratio (1:1:1, 1:2:2, 2:1:1), water/ethanol/acetonitrile), Ni(II) salts ($Ni(BF_4)_2\cdot 6H_2O$, $NiCl_2\cdot 6H_2O$, $Ni(NO_3)_2\cdot 6H_2O$, $Ni(OAc)_2\cdot 4H_2O$, $NiCl_2$), molar ratio, reaction time (30 min, 1h, 3h, and 6h), crystallization techniques (undisturbed solution, slow evaporation, vapor diffusion, solvent diffusion), etc. did not affect the obtained result. Additional experiments were performed in an attempt to favorize either **1a** or **1b**. Ten further reactions were undertaken starting with 1 mL of H_2O and increasing its amount by 1mL in each subsequent reaction with fixed volumes of methanol and acetonitrile (15 mL each). These attempts did not enable the formation of only one complex. Visually, under a microscope, a few crystals of complex **1a** were still found with the majority of **1b**. In the IR spectrum, the two most intense bands are the azide asymmetric stretching vibrations observed at 2053.7 and 2034.2 cm^{-1}. This is conforming with the presence of both end-on bridging and terminal azide [9,10,12,15,18,21,22]. Those bands comply perfectly with the results of DFT calculated vibrations for complex **1b**. The normal modes with the highest calculated IR intensities for **1b** are at 2052.9 and 2030.2 cm^{-1}. These correspond to the asymmetric stretch of bridging and terminal azide, respectively. For **1a**, the azide asymmetric stretching vibrations are calculated to be at 2067.4 and 2017.3 cm^{-1}. This suggests that amount of **1a** is negligible compared to the **1b**.

Further evidence comes from experimentally determined *J* coupling constant that matches *J* calculated for **1b** (Sections 3.3 and 3.5) and from the computational analysis of the energetics of various model systems built from **1a** and **1b** (Section 3.6).

Performing the reaction in dried methanol with anhydrous $NiCl_2$ resulted in the formation of a complex mixture consisting mainly of starting reactants (**HL**Cl ligand precipitated, which was confirmed by elemental analysis and IR spectrum). The role of water molecules is described in X-ray structures of **1a** and **1b** (Section 3.2), as well as by EDA-NOCV analysis (Section 3.6).

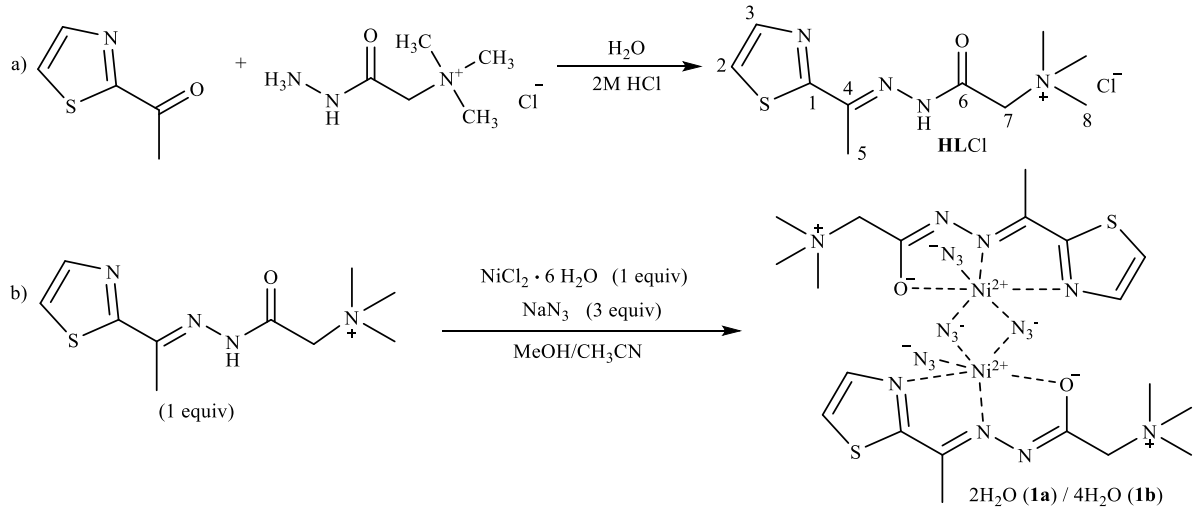

Scheme 2. Synthesis of a) ligand **HL**Cl, b) complexes $[Ni_2\mathbf{L}_2(\mu\text{-}_{1,1}\text{-}N_3)_2(N_3)_2]$.

*3.2. Crystal structures of binuclear $[Ni_2\mathbf{L}_2(\mu\text{-}_{1,1}\text{-}N_3)_2(N_3)_2]\cdot 2H_2O$ (**1a**) and $[Ni_2\mathbf{L}_2(\mu\text{-}_{1,1}\text{-}N_3)_2(N_3)_2]\cdot 4H_2O$ (**1b**) complexes*

The structures of **1a** and **1b** are depicted in Fig. 1, where the numbering schemes adopted for the respective atoms are also given. Selected bond lengths and angles are given in Table 2. The complex units of **1a** and **1b** are neutral dimers of formula $[Ni_2\mathbf{L}_2(\mu\text{-}_{1,1}\text{-}N_3)_2(N_3)_2]$. Complex **1a** crystallizes as the dihydrate in the triclinic crystal system with space group $P\bar{1}$. Complex **1b** crystalizes as the tetrahydrate in the monoclinic crystal system with space group $P2_1/c$. In these complexes, each Ni(II) center is hexacoordinated with the tridentate Schiff base ligand and three azido groups. One azido group is the terminal azido group, while the other two are end-on azido bridges, which form common edge within binuclear units, leading to an edge-sharing bioctahedral

structure. In binuclear complexes **1a** and **1b**, the terminal azido ligands are coordinated in *trans* positions. The N–N–Ni bond angles are 119.6(2)° in **1b** and 123.7(2)° in **1a**, showing bent coordination of the anionic terminals. The terminal azido ligands are nearly linear and slightly asymmetric (N8–N9 = 1.175(4) Å and N9–N10 = 1.151(4) Å for **1a**; N8–N9 = 1.183(3) Å and N9–N10 = 1.164(3) Å for **1b**) with the shorter N(azido)–N(azido) bonds further from the metal center. In **1**, **L** is bonded to Ni(II) through $N_{thiazole}$ (Ni1–N1, 2.126(3) Å in **1a** and 2.122(2) Å in **1b**), N_{imine} (Ni1–N2, 2.017(3) Å in **1a** and 1.997(2) Å in **1b**) and $O_{enolate}$ (2.140(2) Å in **1a** and 2.083(2) Å in **1b**) atoms. The tridentate coordination of each ligand molecule implies the formation of two fused five-membered chelate rings (Ni–N–C–C–N and Ni–N–N–C–O). The chelate rings Ni–N–C–C–N and Ni–N–N–C–O are nearly coplanar in **1a**, as indicated by the dihedral angle of 1.6°. However, the five-membered chelate rings in **1b** show a significant deviation of 4.8° from coplanarity. One of the measures of the octahedral strain is average ΔO_h value. ΔO_h is defined as the mean deviation of 12 octahedral angles from ideal 90°. The Ni1 centers in **1a** show a greater degree of octahedral distortion compared to that in **1b**, as indicated by the average ΔO_h values of 6.92° vs. 6.05°, respectively.

The M–L bond lengths in complexes **1a**, **1b** and analogous $[Ni_2(\mathbf{L^1})_2(\mu_{1,1}\text{-}N_3)_2(N_3)_2]\cdot H_2O\cdot CH_3OH$ [9] ($\mathbf{L^1}$ = (*E*)-*N*,*N*,*N*-trimethyl-2-oxo-2-(2-(quinolin-2-ylmethylene)hydrazinyl)ethan-1-aminium) have been analyzed. The Ni–$N_{quinoline}$ bonds (2.1850(18) Å and 2.1793(19) Å) observed in $[Ni_2(\mathbf{L^1})_2(\mu_{1,1}\text{-}N_3)_2(N_3)_2]\cdot H_2O\cdot CH_3OH$ [9] are longer than the Ni–$N_{thiazole}$ (2.126(3) Å in **1a** and 2.122(2) Å in **1b**). Thus, the Ni–N(heterocycles) bond lengths decrease in the order Ni–N(quinoline) > Ni–N(thiazole). The Ni–N_{imine} bond distances observed in **1a**, **1b**, and $[Ni_2(\mathbf{L^1})_2(\mu_{1,1}\text{-}N_3)_2(N_3)_2]\cdot H_2O\cdot CH_3OH$ [9] are comparable in length and range from 1.9948(17) to 2.017(3) Å. The difference between Ni–$O_{enolate}$ bond lengths in **1a** and **1b** is evident. The Ni–$O_{enolate}$ bond length in **1b** is 2.083(2) Å, while the Ni–$O_{enolate}$ bond in **1a** is longer (2.140(2) Å) and similar to those found in $[Ni_2(\mathbf{L^1})_2(\mu_{1,1}\text{-}N_3)_2(N_3)_2]\cdot H_2O\cdot CH_3OH$ [9] complex (2.0997(15) and 2.1373(16) Å). The difference in Ni–O(enolate) bond lengths may be attributed to different weak interactions (electrostatic and dispersion) present in **1a** and **1b**, and $[Ni_2(\mathbf{L^1})_2(\mu_{1,1}\text{-}N_3)_2(N_3)_2]\cdot H_2O\cdot CH_3OH$ [9] that involve O(enolate) oxygen.

Structural parameters correlating the geometry of the central Ni_2N_2 rings of binuclear complexes **1a** and **1b** are given in Table 3. In these complexes, the central Ni_2N_2 rings are planar

with bridging angles (Ni–$N_{azido(end-on)}$–Ni) of 97.94(8) and 102.08(11)° and Ni···Ni separations of 3.1823(4) and 3.2525(6) Å for **1b** and **1a**, respectively. The Ni–$N_{azido(end-on)}$ bond distances show a discrepancy of 0.019 Å in **1a** and 0.086 Å, in **1b**. In the analyzed complexes, the out-of-plane deviations (δ) of the azide anions are 25.7(2)° (for **1a**) and 44.0(2)° (for **1b**). The Ni–$N_{azido(end-on)}$–Ni bond angles, the Ni–$N_{azido(end-on)}$ bond lengths and Ni···Ni distances observed in binuclear complexes **1a** and **1b** fit into the range of values obtained for the ferromagnetically coupled binuclear tetraazido Ni(II) complexes with tridentate or bis-tridentate ligands (Table S1) [9–22,80]. The complexes analyzed in Table S1 differ in the position of $N_{azido(terminal)}$ atoms with respect to the $Ni_2N_{2(azido(end-on))}$ plane, as evidenced by the $N_{azido(terminal)}$–Ni–$N_{azido(end-on)}$–Ni torsion angles.

In the crystals of **1a** and **1b**, the dimers are assembled into three-dimensional supramolecular structures through intermolecular hydrogen bonds. In the crystals of **1a** the dimeric units are self-assembled into the layers parallel with the (001) lattice plane through C–H···N_{azide}, and C–H···$O_{enolate}$ hydrogen bonds Table S2, Fig. S1a. Solvent water molecule serving as a double donor and double acceptor mediate in joining the neighboring layers in three-dimensional supramolecular structure Table S2, Fig. S1b. In the crystals of **1b**, solvent water molecules (O1w and O2w) form heterodromic water cycles, which serve to connect dimeric units into three-dimensional supramolecular structure Table S3, Fig. S2. The O2w functions as a double donor to O1w and its symmetry equivalent at 2−x, −y, 1−z. The O1w is a double acceptor and double donor to N_{amide} and N_{azide} nitrogens.

Table 2. Selected bond lengths (Å) and angles (°) for complexes **1a** and **1b**.

Complex			
(1a)	Ni1-N1 2.126(3)	N1-Ni1-N2 77.83(11)	N2-Ni1-O1 75.62(10)
	Ni1-N2 2.017(3)	N1-Ni1-N5 103.02(11)	N5-Ni1-O1 103.22(10)
	Ni1-N8 2.070(3)	N1-Ni1-N5^a 91.53(11)	N5^a-Ni1-O1 89.54(10)
	Ni1-N5 2.082(3)	N1-Ni1-N8 91.89(12)	N8-Ni1-O1 92.23(11)
	Ni1-N5^a 2.101(3)	N2-Ni1-N8 94.63(11)	N1-Ni1-O1 153.37(10)
	Ni1-O1 2.140(2)	N2-Ni1-N5^a 96.66(10)	
	N3-C6 1.330(4)	N5-Ni1-N8 90.77(10)	
	O1-C6 1.263(4)	N5-Ni1-N5^a 77.93(11)	
	N8-N9 1.175(4)	N2-Ni1-N5 174.51(9)	
	N9-N10 1.151(4)	N8-Ni1-N5^a 168.66(11)	
	N5-N6 1.193(4)		
	N6-N7 1.151(4)		
(1b)	Ni1-N1 2.122(2)	N1-Ni1-N2 78.46(7)	N2-Ni1-O1 76.86(7)

Ni1-N2	1.997(2)	N1-Ni1-N5	106.35(8)	N5-Ni1-O1	98.08(7)
Ni1-N8	2.109(2)	N1-Ni1-N5^{b}	88.21(8)	N5^{b}- Ni1-O1	90.45(7)
Ni1-N5	2.066(2)	N1-Ni1-N8	94.92(8)	N8-Ni1-O1	89.30(8)
Ni1-N5^{b}	2.152(2)	N2-Ni1-N8	92.06(8)	N1-Ni1-O1	155.09(7)
Ni1-O1	2.083(2)	N2-Ni1-N5^{b}	94.66(7)		
N3-C6	1.331(3)	N5-Ni1-N8	91.09(8)		
O1-C6	1.260(3)	N5-Ni1-N5^{b}	82.06(8)		
N8-N9	1.183(3)	N2-Ni1-N5	174.00(8)		
N9-N10	1.164(3)	N8-Ni1-N5^{b}	173.05(8)		
N5-N6	1.204(3)				
N6-N7	1.150(3)				

Symmetry codes: a = –x+1, –y, –z+1 and b = –x+1, –y, –z.

Table 3. Structural parameters correlating the geometry of the central Ni_2N_2 rings of binuclear complexes **1a** and **1b**.

Complex	Ni–$N_{azido(end\text{-}on)}$–Ni (°)	Ni···Ni (Å)	Ni–$N_{azido(end\text{-}on)}$ (Å)	$N_{azido(terminal)}$–Ni–$N_{azido(end\text{-}on)}$–Ni (°)	δ(°)
(**1a**)	102.08(11)	3.2525(6)	2.101(3); 2.082(3)	-4.5(6); 179.1(1)	25.7(2)
(**1b**)	97.94(8)	3.1823(4)	2.152(2); 2.066(2)	10.2(7); -178.77(8)	44.0(2)

[a] δ(°) is the out-of-plane deviation of the azide ion measured as the angle between Ni_2N_2 plane and the N–N bond.

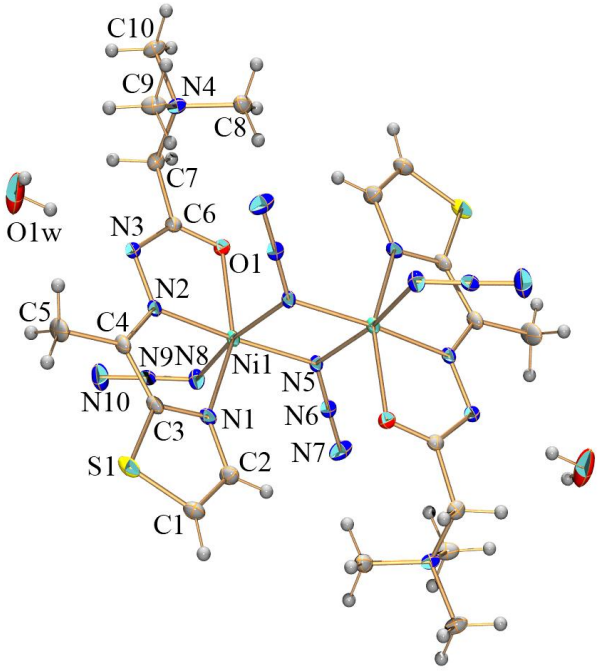

a)

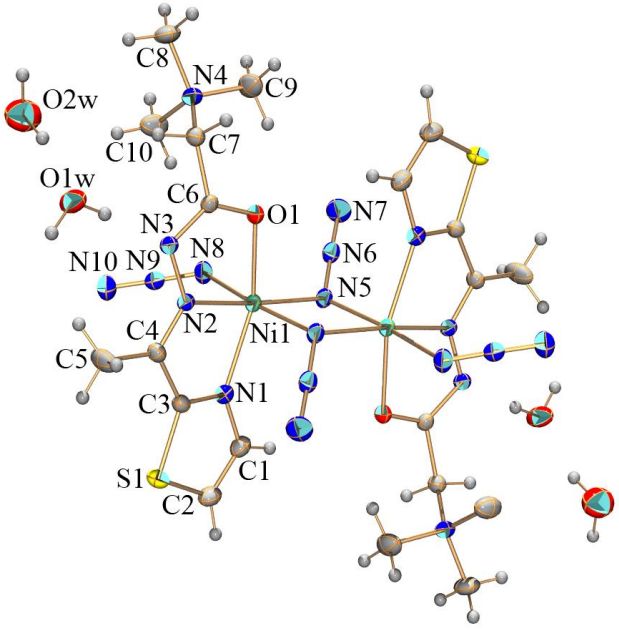

b)

Fig.1. ORTEP presentations of the a) $[Ni_2\mathbf{L}_2(\mu\text{-}_{1,1}\text{-}N_3)_2(N_3)_2]\cdot 2H_2O$ (**1a**) and b) $[Ni_2\mathbf{L}_2(\mu\text{-}_{1,1}\text{-}N_3)_2(N_3)_2]\cdot 4H_2O$ (**1b**). Thermal ellipsoids are drawn at the 30% probability level. Unlabeled part of the dimeric molecules (**1a**) and (**1b**) and the corresponding solvent water molecules are generated by symmetry operations –x+1, –y, –z+1and –x+1, –y, –z, respectively. In (**1a**) H1w from the solvent water molecule, O1w suffers from the positional disorder.

3.3. Magnetic properties

The susceptibility of **1b** (Fig. 2) monotonically increases as temperature decreases from 300 K down to 2 K and, at first glance, resembles a paramagnetic-like 1/*T* dependence. However, the product $\chi \cdot T$ versus temperature (inset in Fig. 3), that should be temperature independent in case of an ideal 1/*T* dependence, reveals interesting magnetic behavior. From the room temperature value of $\chi \cdot T$ = 2.8 emu K/mol, an effective magnetic μ_{eff} = 3.3 μ_B per Ni ion was calculated. This value agrees with the usually measured value of divalent nickel complexes with a nonzero orbital contribution [88]. With decreasing temperature, the product $\chi \cdot T$ starts to increase (indicating dominant ferromagnetic interaction in agreement with theoretical calculations), reaching a maximum at 26.5 K. Bellow 26 K the product $\chi \cdot T$ decreases with decreasing temperature revealing an additional antiferromagnetic interaction in the system.

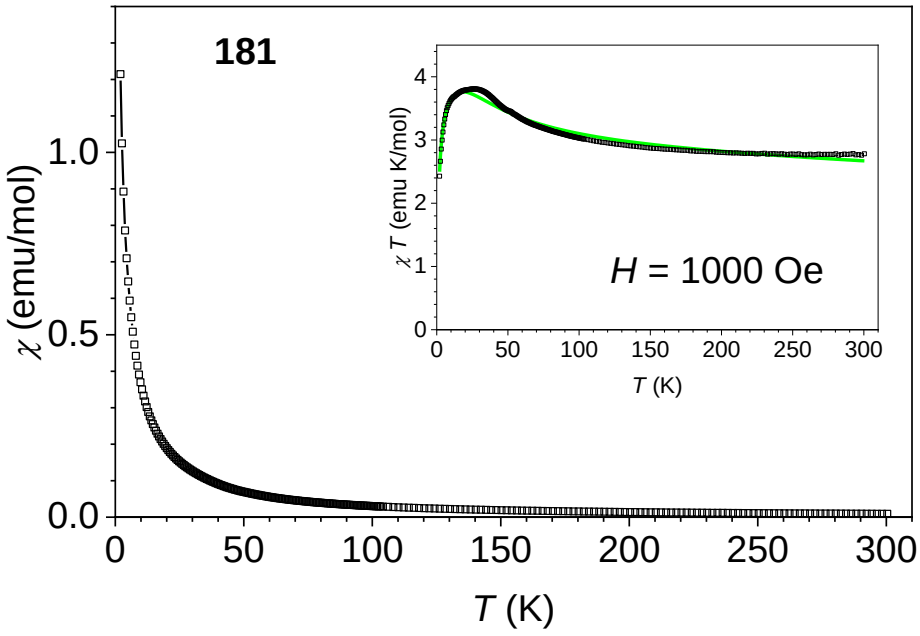

Fig. 2. Temperature dependence of susceptibility χ and product $\chi \cdot T$ (inset) of **1b** measured in a magnetic field of 1 kOe. The full green line is a fit with function (2) and parameters described in the main text.

The measured temperature dependence of the product $\chi \cdot T$ is an excellent example of a binuclear system with ferromagnetic intramolecular interaction J, and antiferromagnetic intermolecular interaction J' between the nearest dimeric units [89]. The corresponding magnetic interaction Hamiltonian can be written as [89]:

$$H_{int} = -2J\,\boldsymbol{S}_A\boldsymbol{S}_B - zJ' < S_z > \boldsymbol{S}_z \qquad (1)$$

with $\boldsymbol{S}_A = \boldsymbol{S}_B = 1$ for Ni(II) ions, and z the number of nearest neighbor units (4 for our structure). The second term describes the intermolecular interactions J' in the molecular-field approximation. Hamiltonian (1) leads to a temperature-dependent susceptibility [89]:

$$\chi = \frac{N_A g^2 \mu_B^2 F(J,T)}{k_B T - zJ' F(J,T)} \qquad (2)$$

where constant N_A, g, k_B, and μ_B acquire their usual meaning. For binuclear Ni(II) units, the function $F(J,T)$ is:

$$\boldsymbol{F(J,T)} = \mathbf{2}\,\frac{\boldsymbol{e^x + 5e^{3x}}}{\mathbf{1 + 3e^x + 5e^{3x}}} \qquad (3)$$

with $x = 2J/(k_B T)$. The best fit of the experimental data with function (2) in the form of the product $\chi \cdot T(T)$ was obtained with parameters $g = 2.3$, $J = 9.5$ cm^{-1}, $J' = -0.12$ cm^{-1} and is shown as a full green line in the inset in Fig. 2.

3.4. Assessment of DFAs for calculation of the exchange coupling

Binuclear complexes **I–XIX**, used for the assessment of DFAs for the calculation of J values, have magnetic coupling in the range -1.77-+36.3 cm^{-1}. Complexes **I–XVII** share common structural motif - Ni(II) centers are octahedrally coordinated with two end-on azide bridged ligands and one terminal azide ligand. Ni-N-Ni bridging angles are between approx. 98° and 103.9°, Ni---Ni distances between 3.155 and 3.448 Å (Table S1). Ferromagnetic coupling is typical for the double end-on azide bridged binuclear Ni(II) complexes [1,2]. The exception is when a low Ni-N-Ni bridge angle and shorter Ni---Ni separation lead to weak antiferromagnetic coupling, as found in the complex **XVIII** (Ni-N-Ni angle 90.4°, Ni---Ni distance 3.011 Å, and J=−1.77 cm^{-1}) [58].

Calculated *J* values by different DFAs are presented in Tables 4–6. Table 4 summarizes the results obtained by GGAs (BP86, BLYP, OLYP, OPBE) and meta-GGAs (M06-L and TPSS); Table 5 reports the results by hybrid (B3LYP, B3LYP*, BHandHLYP) and meta-hybrid functionals (M06, M06-2X, and TPSSh). In Table 6, results by double-hybrid (B2PLYP and PWPB95) functionals are given. Irrespectively of the choice of DFA, the qualitatively correct ferromagnetic coupling is obtained in cases **I**–**XVII** and **XIX**. However, complex **XVIII** is more troublesome for the BS-DFT predictions. Except for double-hybrids (B2PLYP and PWPB95), all DFAs fail to predict weak antiferromagnetic coupling for complex **XVIII**. A quantitative agreement depends on DFA employed. In general, only double-hybrid functionals gave the mean absolute error (MAE) less than 10 cm^{-1}. GGAs and meta-GGAs gave similar results (Table 4) with MAE around 25 cm^{-1}, overestimating the ferromagnetic interactions. The results are also somewhat divergent, with a span of errors between 6 and 43 cm^{-1}. Inclusion of modest amount of the exact exchange in hybrid and meta-hybrid DFAs (10% in TPSSh, 15% in B3LYP*, 20% in B3LYP, 27% in M06) does not improve the results (Table 5). DFAs with a higher percentage of the exact exchange (50% in BHandHLYP and 54% in M06-2X) lead to less overestimation of the ferromagnetic interactions. Meta-hybrid M06-2X gives the best results among chosen "standard DFAs" (Table 4 and Table 5), with MAE of 11 cm^{-1} and a span of absolute errors between 0.90 and 28 cm^{-1}. Double-hybrid functionals demonstrate definite improvement over other chosen functionals (Table 6). PWPB95 is the best of all 14 selected functionals with MAE of 6.5 cm^{-1}, and maximal AE of 15 cm^{-1}. Only in four complexes (**IV**, **VII**, **XI, XV**) calculated *J* differ from the experimentally estimated values by more than 10 cm^{-1}. It is noteworthy to mention that this behavior of double-hybrids is not necessarily universal. Double-hybrid functionals show excellent results in energetics [74,90–94]. However, they are seldomly used for the calculation of magnetic coupling [38,39,43,95,96], and not always giving an improvement compared to the hybrid functionals [38,39]. *J* coupling calculated with double-hybrid functionals without perturbational correction, i.e., DFT only values, are similar to the calculated values by hybrid functionals with a high percentage of the exact exchange (Table 6). The apparent reason is the high admixture of the exact exchange in double-hybrid functionals - 53% in B2PLYP and 50% in PWPB95. B2PLYP DFT only calculated values are almost the same as the BHandHLYP ones. Perturbational contribution to the exchange coupling (ΔJ_{PT2}) corrects the overestimation of the ferromagnetic interactions, and in the PWPB95 case in a somewhat more balanced way (Table 6).

Table 4. Exchange coupling constants (in cm^{-1}) calculated with selected GGAs and meta-GGAs for 17 Ni(II) binuclear complexes and comparison with experimentally determined values. Mean error (ME), mean absolute error (MAE), minimal absolute error (Min AE), and maximal absolute error (Max AE) in cm^{-1}.

Complex	Exp.	BP86	BLYP	OLYP	OPBE	M06-L	TPSS
I	12.00 [9]	50.50	49.48	51.9	52.92	46.73	53.45
II	34.20 [10]	54.48	52.93	57.39	58.58	49.2	53.84
III	11.35 [10]	42.945	42.82	46.465	47.63	37.23	41.76
IV	1.91 [11]	28.285	27.425	29.815	26.565	29.95	30.68
V	28.32 [12]	54.71	56.06	55.31	53.21	5.21	54.88
VI	25.50 [13]	47.78	46.31	47.19	49.71	45.95	50.27
VII	36.30 [14]	43.29	42.09	43.79	44.5	42.45	45.72
VIII	22.80 [15]	45.98	44.87	45.07	45.89	47.85	50.36
IX	23.35 [16]	32.00	30.31	29.47	31.63	31.38	34.90
X	18.61 [17]	51.30	50.10	52.88	54.53	43.69	49.88
XI	31.87 [17]	45.39	44.18	48.3	49.01	38.21	43.18
XII	16.87 [18]	46.04	45.47	49.24	49.87	39.88	41.27
XIII	33.00 [19]	73.57	72.06	74.69	75.875	60.84	74.08
XIV	24.90 [20]	59.68	57.91	58.71	60.15	54.02	60.43
XV	6.12 [80]	47.42	48.47	45.11	43.77	38.48	43.29
XVI	21.80 [21]	49.05	47.64	50.76	51.95	46.75	50.65
XVII	20.96 [22]	37.95	36.98	38.93	39.82	35.04	38.06
XVIII	-1.77 [58]	11.93	11.05	20.71	20.91	12.97	11.34
XIX	13.85 [58]	35.67	34.84	41.47	41.93	30.94	33.46
ME		25.05	24.16	26.24	27.18	18.68	25.24
MAE		25.05	24.16	26.24	27.18	21.11	25.24
Min AE		6.99	5.79	6.12	8.20	6.15	9.42
MAX AE		41.30	42.35	41.69	42.88	34.73	41.45

Table 5. Exchange coupling constants (in cm^{-1}) calculated with selected hybrid and meta-hybrid DFAs for 17 Ni(II) binuclear complexes and comparison with experimentally determined values. Mean error (ME), mean absolute error (MAE), minimal absolute error (Min AE), and maximal absolute error (Max AE) in cm^{-1}.

Complex	Exp.	B3LYP	B3LYP*	BHandHLYP	M06	M06-2X	TPSSh
I	12.00 [9]	55.41	55.22	51.04	55.91	40.45	56.72
II	34.20 [10]	53.73	55.65	39.08	57.07	32.26	53.83
III	11.35 [10]	39.045	42.22	27.95	43.42	25.12	40.93
IV	1.91 [11]	35.425	34.96	29.86	39.89	25.66	35.99
V	28.32 [12]	35.30	31.10	30.55	54.26	27.42	28.63
VI	25.50 [13]	56.10	57.18	44.02	58.10	36.90	53.83
VII	36.30 [14]	49.91	51.55	42.84	53.59	34.94	50.05
VIII	22.80 [15]	58.71	59.66	52.20	61.05	41.85	57.18
IX	23.35 [16]	40.05	40.03	34.80	44.21	28.86	39.33
X	18.61 [17]	46.31	48.92	33.82	52.03	29.87	49.51
XI	31.87 [17]	38.56	40.50	27.88	43.76	24.46	42.47
XII	16.87 [18]	36.45	36.49	30.84	42.71	26.67	37.40
XIII	33.00 [19]	71.03	72.18	55.81	71.67	45.14	74.69
XIV	24.90 [20]	61.98	62.98	46.45	64.38	38.07	62.63
XV	6.12 [80]	38.31	40.9	30.87	42.34	26.18	30.21
XVI	21.80 [21]	52.00	52.99	43.24	62.06	36.69	52.56
XVII	20.96 [22]	39.63	39.65	31.30	43.37	27.52	39.52
XVIII	-1.77 [58]	10.03	11.92	4.74	16.07	2.36	12.2
XIX	13.85 [58]	29.00	31.31	21.81	36.37	19.09	28.77
ME		24.48	25.45	15.64	29.49	9.87	24.45
MAE		24.48	25.45	16.06	29.49	11.09	24.45
Min AE		6.69	2.78	2.23	11.89	0.90	0.31
MAX AE		43.41	43.22	39.04	43.91	28.45	44.72

Table 6. Exchange coupling constants (in cm^{-1}) calculated with double-hybrid B2PLYP and PWPB95 for 17 Ni(II) binuclear complexes and comparison with experimentally determined values. Mean error (ME), mean absolute error (MAE), minimal absolute error (Min AE), and maximal absolute error (Max AE) in cm^{-1}. DFT only values and perturbational contribution ΔJ_{PT2} are given as well.

Complex	Exp.	B2PLYP (DFT)	B2PLYP	PWPB95 (DFT)	PWPB95	ΔJ_{PT2} (B2PLYP)	ΔJ_{PT2} (PWPB95)
I	12.00 [9]	52.60	0.58	46.82	18.22	-52.02	-28.6
II	34.20 [10]	37.94	25.05	37.44	29.18	-12.89	-8.26
III	11.35 [10]	28.29	17.49	27.13	16.78	-10.81	-10.36
IV	1.91 [11]	30.41	14.02	28.38	16.33	-16.39	-12.05
V	28.32 [12]	35.34	18.97	29.44	20.20	-16.37	-9.24
VI	25.50 [13]	43.66	28.17	41.84	28.10	-15.49	-13.74
VII	36.30 [14]	43.02	21.01	39.01	24.21	-22.01	-14.80
VIII	22.80 [15]	52.81	15.60	48.25	26.57	-37.21	-21.68
IX	23.35 [16]	37.42	20.27	31.46	20.16	-17.15	-11.30
X	18.61 [17]	33.82	23.17	32.01	23.10	-10.65	-8.91
XI	31.87 [17]	27.77	19.14	25.75	17.52	-8.63	-8.23
XII	16.87 [18]	31.19	3.31	30.04	19.64	-27.88	-10.40
XIII	33.00 [19]	56.06	24.16	51.83	30.11	-31.90	-21.73
XIV	24.90 [20]	46.25	29.15	44.00	30.52	-17.10	-13.48
XV	6.12 [80]	29.93	21.97	28.94	21.04	-7.96	-7.90
XVI	21.80 [21]	42.92	30.09	41.21	28.58	-12.83	-12.63
XVII	20.96 [22]	31.24	18.29	30.39	19.56	-12.95	-10.83
XVIII	-1.77 [58]	5.48	-8.29	3.98	-6.54	-13.77	-10.52
XIX	13.85 [58]	22.06	8.75	20.09	9.74	-13.31	-10.35
ME		16.12	-2.69	13.48	0.58		
MAE		16.55	8.36	14.12	6.47		
Min AE		3.74	2.67	1.12	1.40		
MAX AE		40.60	15.85	34.82	14.92		

The trend of the results (Tables 4–6), at first sight, seems in contrast to the typical behavior of DFAs. It is expected that GGAs favor low spin states, while hybrid DFAs stabilize the high-spin states. This anticipation does not take into account the details of the magnetic coupling. The ferromagnetic coupling can be understood based on the analysis of the unrestricted corresponding orbitals [97] obtained from the broken-symmetry determinant. Magnetic orbitals centered on each of the Ni(II) are local $d_{x^2-y^2}$ and d_{z^2} orbitals. The poor overlap of the pairs of magnetic orbitals (calculated overlap is always less than 0.1), as dictated by the geometry of the binuclear complexes, is hindering the antiferromagnetic coupling [98]. The spin density in the ferromagnetic state of studied compounds is located mainly on the Ni(II) centers (Table S4). The localization of the spin density follows a common tendency. GGA functionals overestimate delocalization [99]. In contrast, the extent of the localization is more significant, with a higher percentage of the exact exchange in hybrid functionals [100] (Table S4). Accordingly, GGA functionals have a bias toward the ferromagnetic coupling in studied systems (Table 4). In hybrid functionals, two opposing aspects come into play - localization of the spin density that lowers ferromagnetic coupling and higher correlation of the unpaired electrons that stabilize the high-spin state. Double-hybrid functionals improve most of the shortcomings of other DFAs. The high percentage of the exact exchange localizes the spin density. At the same time, perturbational correction fixes the issue of the overstabilization of the high-spin states (ΔJ_{PT2}, Table 6, stabilizes the low-spin state), i.e., reducing further the ferromagnetic coupling. It is noticeable that PWPB95, which overall has the best behavior in studied systems, regards the correlation contribution of opposite-spin electron pairs solely.

*3.5. Exchange coupling in **1a** and **1b***

The exchange coupling in binuclear complexes **1a** and **1b** has been calculated by the BS-DFT approach with M06-2X, B2PLYP, and PWPB95 functionals (Table 7). The computed values for **1b** with B2PLYP and PWPB95 functionals are in excellent agreement with the experiment. The *J* is overestimated by approx. 4.5 cm^{-1}, similarly to the results presented above for other binuclear complexes (Table 6). Geometries of **1a** and **1b** are comparable to geometries of other ferromagnetic systems **I**–**XVII** (Table 3 and Table S1).

Table 7. Exchange coupling constants (in cm^{-1}) calculated with meta-hybrid M06-2X and double-hybrid B2PLYP and PWPB95 for Ni(II) binuclear complexes **1a**, and **1b**, and comparison with experimentally determined values. DFT only values for double-hybrids are given as well.

Complex	Exp.	M06-2X	B2PLYP (DFT)	B2PLYP	PWPB95 (DFT)	PWPB95
1a	9.5	34.78	40.94	24.46	37.70	25.40
1b		20.68	24.21	13.78	22.53	13.97

The spin density in the ground ferromagnetic state is localized around Ni(II) centers. The slight delocalization toward the directly coordinated ligand atoms and terminal nitrogen atoms of the bridging azides is observed (Fig.3). All atoms bearing apparent spin density have the same sign, pointing out to the spin delocalization as the primary exchange mechanism.

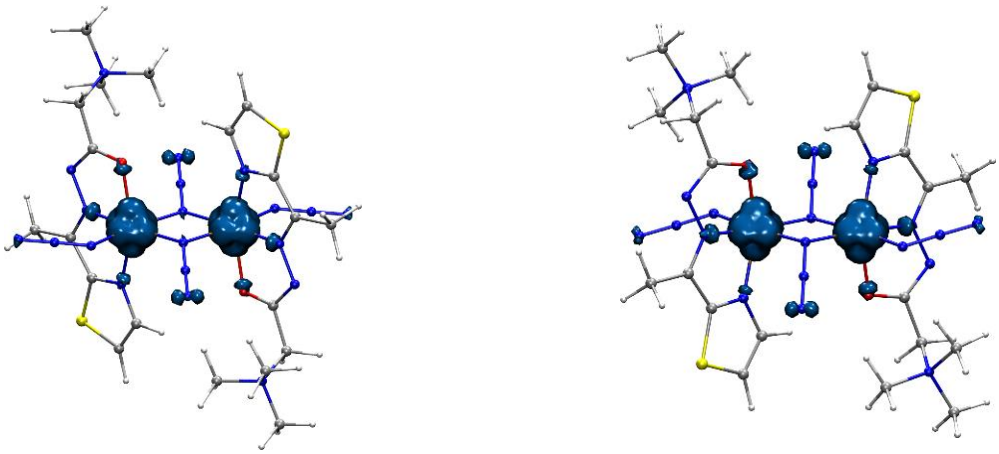

1a **1b**

Fig.3. Graphical representation of the spin density of the high-spin state of the binuclear complexes **1a** and **1b**. Isosurfaces were drawn at 0.01 e/$Å^3$ with blue surfaces representing α-spin.

Each Ni(II) center is in the local octahedral environment (X-ray part), with local S = 1 electronic state (d^8 local electronic configuration). Unpaired electrons are placed in the local

$d_{x^2-y^2}$ and d_{z^2} orbitals. Pairs of the unrestricted corresponding orbitals [97] obtained from the broken-symmetry determinants are depicted in Fig.4. The poor overlap between magnetic orbitals in each pair implies that antiferromagnetic coupling is quenched. Equivalent interactions were reported previously in **I** [9].

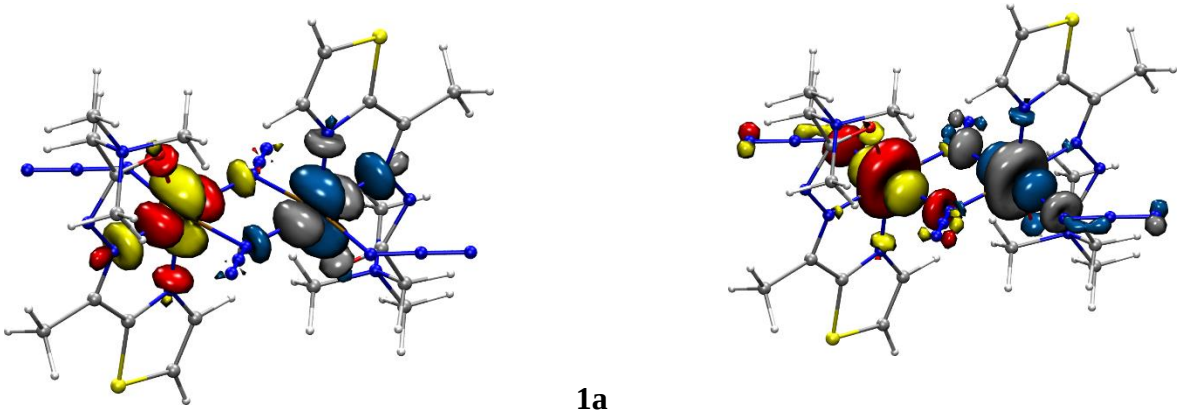

1a

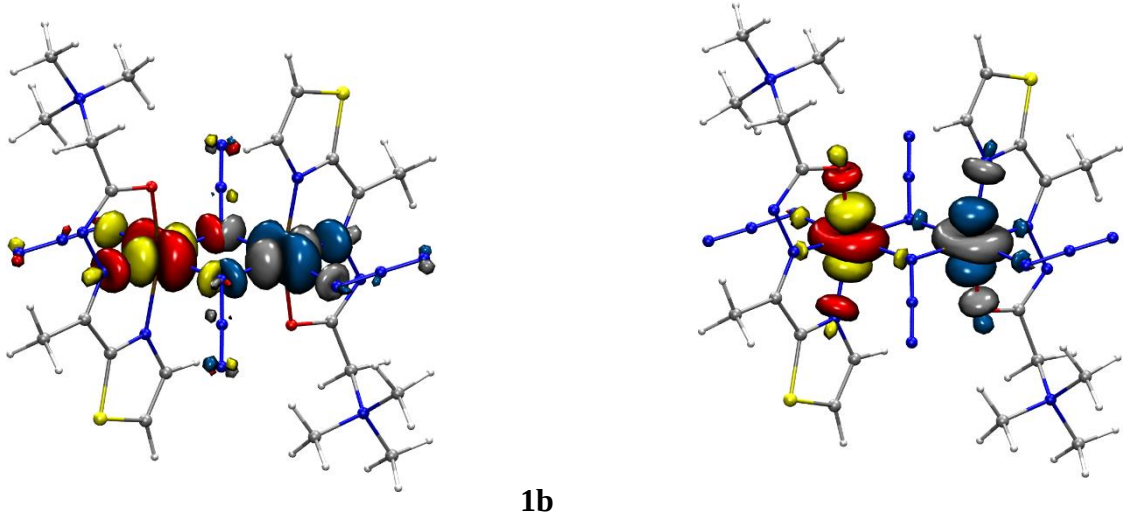

1b

Fig.4. Corresponding orbitals obtained from the broken-symmetry solution of the binuclear complexes **1a** and **1b**. α spin-orbitals are depicted as red (positive)/yellow (negative) lobes; β spin-orbitals are depicted as blue (positive)/grey (negative) lobes. Isosurfaces were drawn at 0.04 e/Å^3. Their spatial overlaps are: 0.00026 and 0.00169 (**1a**); 0.00389 and 0.00186 (**1b**),

*3.6. Computational analysis of structures **1a** and **1b***

To rationalize the fact that **1b** is a dominant product regardless of experimental conditions (Section 3.1), we have performed BP86-D3/ZORA-def2-TZVP(-f), B3LYP-D3/ZORA-def2-TZVP(-f), M06-2X/ZORA-def2-TZVP(-f), and ZORA-BP86-D4/TZP calculations on model systems build from corresponding X-ray structures, which vary in a number of H_2O molecules. The simplest models are bare $[Ni_2\mathbf{L}_2(\mu\text{-}_{1,1}\text{-}N_3)_2(N_3)_2]$ units. The largest considered models are dimers of binuclear units with all crystal waters present (four in **1a** dimer and eight in **1b** dimer). All the model systems are depicted in Fig. S4. The chosen modes systems are: i) **1a*** and **1b***, i.e., $[Ni_2\mathbf{L}_2(\mu\text{-}_{1,1}\text{-}N_3)_2(N_3)_2]$ complexes from corresponding crystal structures without lattice H_2O; ii) **1a** (crystal structure of $[Ni_2\mathbf{L}_2(\mu\text{-}_{1,1}\text{-}N_3)_2(N_3)_2]\cdot 2H_2O$) and **1b***$\cdot 2H_2O$; iii) **1a** + $2H_2O$ and **1b** (crystal structure of $[Ni_2\mathbf{L}_2(\mu\text{-}_{1,1}\text{-}N_3)_2(N_3)_2]\cdot 4H_2O$); iv) **1a***--$(H_2O)_2$--**1a*** + $2H_2O$ (two 1a* molecules connected via water dimer and two additional water molecules) and **1b***--$(H_2O)_4$--**1b*** (two 1b* molecules connected via water tetramer); (v) $(\mathbf{1a})_2$ + $4H_2O$, (a dimer of **1a** taken from the crystal structure and four additional water molecules) and $(\mathbf{1b})_2$, i.e., a dimer of **1b** made from the crystal structure. In this way, we can compare energies of model systems based on **1a** and **1b** with an equal number of atoms, Table 8. The results reveal that in all cases, model systems based on **1b** have lower energies than those based on **1a**. In the case of optimized structures of **1a*** and **1b*** (at BP86-D4/TZP level of theory), **1b*** is lower in energy for 6.6 kcal/mol.

Table 8. Energies (in kcal/mol) of model systems constructed from X-ray structures of **1a** and **1b** at different levels of theory.

	1a*/1b*	**1a/1b***$\cdot 2H_2O$	**1a**+$2H_2O$/**1b**	**1a***--$(H_2O)_2$--**1a*** + $2H_2O$ / **1b***--$(H_2O)_4$--**1b***	$(\mathbf{1a})_2$ + $4H_2O$ / $(\mathbf{1b})_2$
BP86-D3/def2-TZVP(-f)[a]	12.6/0.0	9.4/0.0	34.9/0.0	44.1/0.0	66.7/0.0
B3LYP-D3/def2-TZVP(-f)[a]	10.6/0.0	7.1/0.0	32.5/0.0	39.7/0.0	61.6/0.0
M06-2X/def2-TZVP(-f)[a]	10.5/0.0	5.7/0.0	29.8/0.0	37.4/0.0	56.4/0.0
BP86-D4/TZP[b]	12.5/0.0	11.5/0.0	32.5/0.0	41.1/0.0	61.9/0.0

[a] Calculations with ORCA program package [b] Calculations with ADF program package

EDA analysis, Table 9, is performed to understand the formation of supramolecular structures. For this purpose, the interaction energy between two monomeric units of [Ni_2**L**$_2$(μ-$_{1,1}$-N_3)$_2$(N_3)$_2$] and water clusters between them, from the X-ray structures was investigated. The interaction energy between three fragments is lower (i.e., more negative) for the model system taken from **1b**.

Table 9. Energy Decomposition Analysis at BP86-D4/TZP level of theory for the formation of dimeric structures of **1a** and **1b**; model systems are constructed from X-ray structures of **1a** and **1b**; energy components are given in kcal/mol relative to the chosen fragments; dashed lines indicate fragmentation; energy components per bond are shown in brackets.

	E_{Elst}	E_{Pauli}	E_{Orb}	E_{σ}[a]	E_{disp}	E_{Int}
1a*--$(H_2O)_2$--**1a***	-41.92	46.56	-27.49	-16.37	-10.96	-33.81
	(-20.96)	(23.28)	(-13.75)	(-8.19)	(-5.48)	(-16.91)
[(H_2O)**1a***]--$(H_2O)_2$--[**1a***(H_2O)][b]	-41.78	46.53	-27.5	-16.38	-10.96	-33.71
	(-20.89)	(23.27)	(-13.75)	(-8.19)	(-5.48)	(-16.86)
1b*--$(H_2O)_4$--**1b***	-45.5	46.90	-33.48	-21.37	-11.89	-43.97
	(-22.75)	(23.45)	(-16.74)	(-10.69)	(-5.95)	(-21.99)
[$(H_2O)_2$**1b***]--$(H_2O)_4$--[**1b***$(H_2O)_2$][c]	-45.27	46.85	-33.48	-21.34	-11.90	-43.80
	(-22.64)	(23.43)	(-16.74)	(-10.67)	(-5.95)	(-21.90)

[a]Part of E_{Orb} corresponding to σ covalent bond between fragments. [b] Corresponds to dimer (**1a**)$_2$; [c] Corresponds to dimer (**1b**)$_2$.

In all the structures, the electrostatic interaction between the chosen fragments accounts for 50% of the stabilization, and orbital interaction gives around 35% of the stabilization. Dispersion correction is non-negligible (15% of stabilization). NOCV analysis disclosed that dominant electron density flow channels represent σ-covalent hydrogen bonding between water and monomer units, Fig. 5. This σ-covalent interaction brings 20% of stabilization to the system based on **1a** and 23% of stabilization to the system based on **1b**. The rest of the orbital stabilization is due to the polarization. Pauli interaction and dispersion corrections are similar in models based on both **1a** and **1b**. The difference in interaction energies in dimer models of **1a** and **1b** stems from the electrostatic contribution and the σ covalency. Thus, EDA-NOCV analysis unveils that two additional water molecules in **1b** have a synergistic effect on the interaction between monomer units. This is additionally confirmed by EDA-NOCV analysis of the interaction of water molecules

and monomer units (**1a***--H_2O**, 1b***--H_2O**,** and **1b***--$(H_2O)_2$, Table S5, Fig. S5). The EDA-NOCV analysis /Table 9, Fig. 5), together with energies of model systems (Table 8), explains the predominant formation of **1b**.

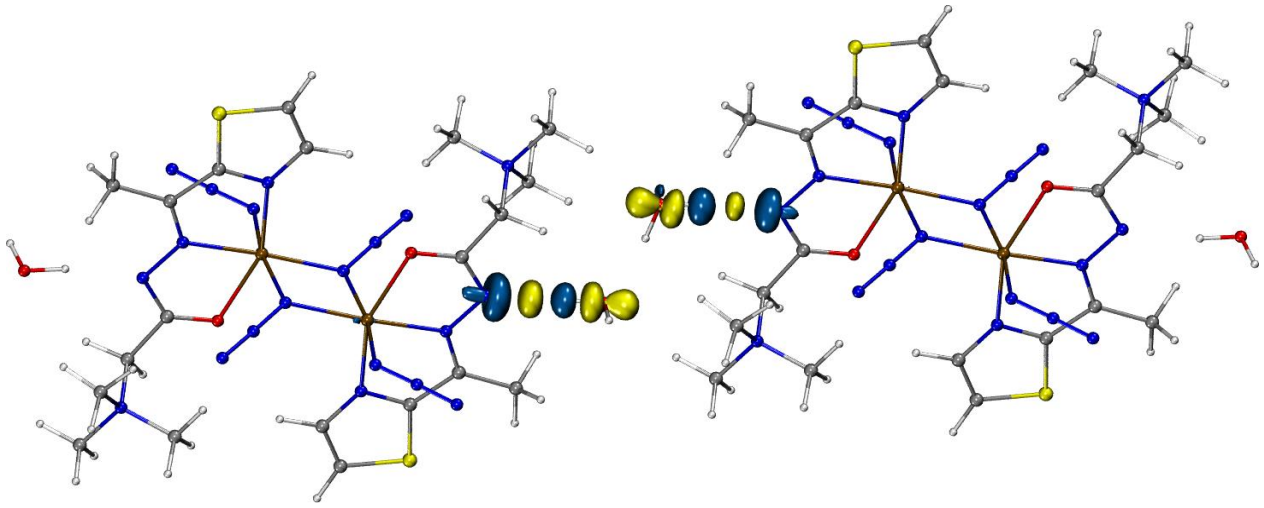

[(H_2O)**1a***]--$(H_2O)_2$--[**1a***(**)**H_2O)] E_σ = -16.4 kcal/mol

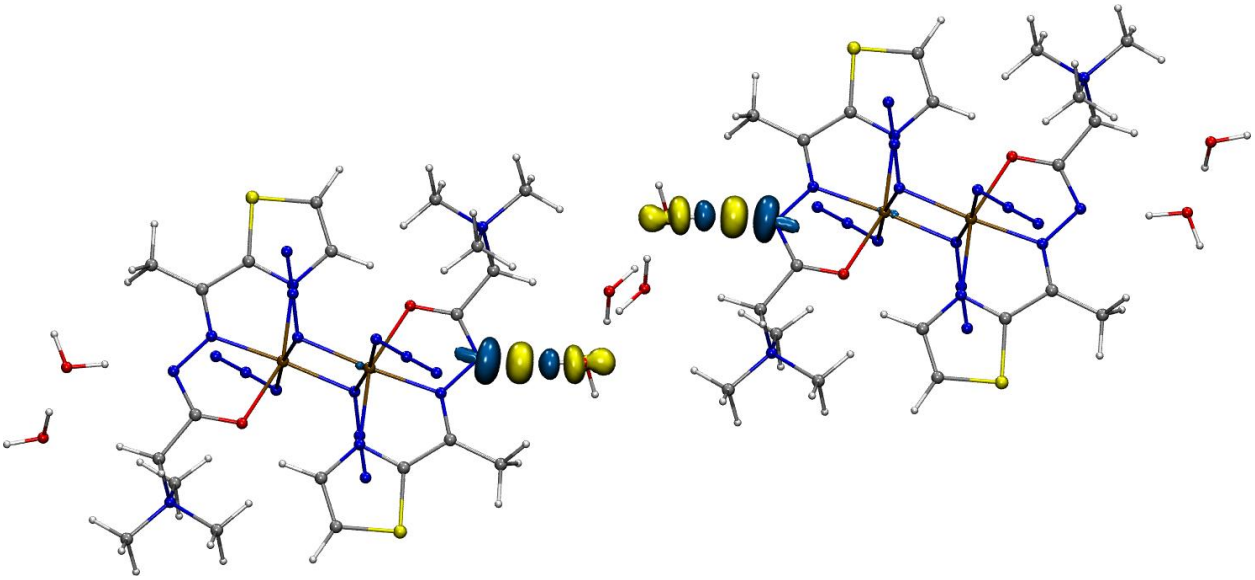

[$(H_2O)_2$**1b***]--$(H_2O)_4$--[**1b***$(H_2O)_2$] E_σ = -21.4 kcal/mol

Fig. 5 Most important density deformation channels from EDA–NOCV analysis of the formation of dimeric structures of **1a** (up) and **1b** (down). Their relevance is given by their energy contribution E_σ to E_{orb}. Charge outflow/inflow is represented by yellow/blue color (isovalue = 0.004 a.u.)

4. Conclusions

In the reaction of the ligand (*E*)-*N*,*N*,*N*-trimethyl-2-oxo-2-(2-(1-(thiazol-2-yl)ethylidene)hydrazinyl)ethan-1-aminium chloride (**HL**Cl) with $NiCl_2 \cdot 6H_2O$ and NaN_3 in molar ratio 1:1:3 in methanol/acetonitrile mixture of solvents, a binuclear double end-on azido bridged Ni(II) complex (**1b**), with composition $[Ni_2\mathbf{L}_2(\mu\text{-}_{1,1}\text{-}N_3)_2(N_3)_2] \cdot 4H_2O$, together with complex **1a** $[Ni_2\mathbf{L}_2(\mu\text{-}_{1,1}\text{-}N_3)_2(N_3)_2] \cdot 2H_2O$ (few crystals), have been obtained from the same solution. Complexes were characterized by single-crystal X-ray crystallography. Complex **1a** crystallizes as the dihydrate in the triclinic crystal system with space group $P\bar{1}$ and complex **1b** as the tetrahydrate in the monoclinic crystal system with space group $P2_1/c$. In these complexes, each Ni(II) center is hexacoordinated with the tridentate Schiff base ligand and three azido groups. One azido group is the terminal azido group, while the other two are end-on azido bridges, which form common edge within binuclear units, leading to an edge-sharing bioctahedral structure. Variable-temperature magnetic susceptibility measurements showed ferromagnetic intramolecular interaction between Ni(II) ions. The *J* value, as well as the $Ni–N_{azido(end\text{-}on)}–Ni$ bond angles, the $Ni–N_{azido(end\text{-}on)}$ bond lengths and Ni···Ni distances, are in accordance with values obtained for the similar, 17 ferromagnetically coupled binuclear tetraazido Ni(II) complexes. A comprehensive BS-DFT study revealed the importance of the choice of DFT functionals for the calculation of *J* in end-on azido bridged binuclear Ni(II) complexes. For this purpose, 14 DFAs with different flavors were selected (GGAs, meta-GGAs, hybrid functionals, meta-hybrid functionals, and double-hybrid functionals). These 14 exchange-correlation functionals were used for the calculations of *J* constants in 19 structurally related binuclear Ni(II) complexes, for which the *J* value was determined experimentally. We believe that this validation study will be useful as a guideline for future studies on these types of systems. It was shown that binuclear double end-on azido bridged Ni(II) complexes are challenging for theoretical description, as most of herein used DFAs overestimate ferromagnetic interactions. Only double-hybrid functionals were able to predict rare, weak antiferromagnetic coupling in complex **XVIII**. The main disadvantage of double-hybrid functionals is their high computational cost. However, in herein systems, this is worth the effort as they show MAE bellow 9 cm^{-1} in the entire set. This collection of binuclear complexes, or part of this collection, may be included in the future, more extensive, and diverse benchmark sets for the judgment of the quality of DFAs on the calculation of the exchange coupling. Based on this assessment, three DFAs were chosen for the calculation of *J* constant in

1a and **1b**, namely meta-hybrid M06-2X and double-hybrid B2PLYP and PWPB95. The calculated *J* value for **1b** agrees with experimentally determined *J* value. BS-DFT calculations explained ferromagnetic exchange coupling in the examined complexes. Lastly, EDA-NOCV analysis rationalized the role of crystal water molecules in structures **1a** and **1b**. Crystal water molecules are not innocent bystanders but are serving as mediators in the formation of supramolecular structures in the crystals of **1a** and **1b**. The present results demonstrate that synergy between experimental and computational chemistry is necessary for understanding the structure and properties of inorganic complexes.

Acknowledgements

This work was financially supported by the Ministry of Education, Science and Technological Development of the Republic of Serbia (Grant No. 451-03-68/2020-14/200168 and 451-03-68/2020-14/200026) and Slovenian Research Agency (P1-0175 and P2-0348). We thank the EN-FIST Centre of Excellence, Ljubljana, Slovenia, for the use of the SuperNova diffractometer.

Appendix A. Supplementary data

CCDC 2009327 (for **1a**) and 2009328 (for **1b**) contain the supplementary crystallographic data for this paper. These data can be obtained free of charge fromThe Cambridge Crystallographic Data Centre via www.ccdc.cam.ac.uk/data_request/cif. Supplementary data to this article can be found online at https:

References

[1] J. Ribas, A. Escuer, M. Monfort, R. Vicente, R. Corteś, L. Lezama, T. Rojo, Coord. Chem. Rev. 193–195 (1999) 1027–1068.

[2] E. Ruiz, J. Cano, S. Alvarez, P. Alemany, J. Am. Chem. Soc. 120 (1998) 11122–11129.

[3] B. Machura, J.G. Małecki, A. Świtlicka, I. Nawrot, R. Kruszynski, Polyhedron 30 (2011) 864–872.

[4] M.R. Milenković, A.T. Papastavrou, D. Radanović, A. Pevec, Z. Jagličić, M. Zlatar, M. Gruden, G.C. Vougioukalakis, I. Turel, K. Anđelković, B. Čobeljić, Polyhedron 165 (2019) 22–30.

[5] S. Naiya, C. Biswas, M.G.B. Drew, C.J. Gómez García, J.M. Clemente-Juan, A. Ghosh, Inorg. Chem. 49 (2010) 6616–6627.

[6] J.-P. Zhao, B.-W. Hu, E.C. Sañudo, Q. Yang, Y.-F. Zeng, X.-H. Bu, Inorg. Chem. 48 (2009) 2482–2489.

[7] L.-F. Zhang, M.-M. Yu, Z.-H. Ni, A.L. Cui, H.-Z. Kou, J. Mol. Struct. 1006 (2011) 629–634.

[8] C.-B. Tian, Z.-H. Li, J.-D. Lin, S.-T. Wu, S.-W. Du, P. Lin, Eur. J. Inorg. Chem. 2010, 427–437.

[9] M.Č. Romanović, B.R. Čobeljić, A. Pevec, I. Turel, V. Spasojević, A.A. Tsaturyan, I.N. Shcherbakov, K.K. Anđelković, M. Milenković, D. Radanović, M.R. Milenković, Polyhedron 128 (2017) 30–37.

[10] S. Sarkar, A. Mondal, M.S. El Fallah, J. Ribas, D. Chopra, H. Stoeckli-Evans, K.K. Rajak, Polyhedron 25 (2006) 25–30.

[11] H.-D. Bian, W. Gu, Q. Yu, S.-P. Yan, D.-Z. Liao, Z.-H. Jiang, P. Cheng, Polyhedron 24 (2005) 2002–2008.

[12] S. Liang, Z. Liu, N. Liu, C. Liu, X. Di, J. Zhang, J. Coord. Chem. 63 (2010) 3441–3452.

[13] S.S. Massoud, F.R. Louka, Y.K. Obaid, R. Vicente, J. Ribas, R.C. Fischer, F.A. Mautner, Dalton Trans. 42 (2013) 3968–3978.

[14] R. Cortés, J.I. Ruiz de Larramendi, L. Lezama, T. Rojo, K. Urtiaga, M.I. Arriortua, J. Chem. Soc. Dalton Trans. (1992) 2723–2728.

[15] M.G. Barandika, R. Cortés, L. Lezama, M.K. Urtiaga, M.I. Arriortua, T. Rojo, J. Chem. Soc., Dalton Trans. (1999) 2971−2976.

[16] A. Escuer, R. Vicente, J. Ribas, X. Solans, Inorg. Chem. 34 (1995) 1793–1798.

[17] A. Solanki, M. Monfort, S.B. Kumar, J. Mol. Struct. 1050 (2013) 197–203.

[18] S. Nandi, D. Bannerjee, J.-S. Wu, T.-H. Lu, A.M.Z. Slawin, J.D. Woollins, J. Ribas, C. Sinha, Eur. J. Inorg. Chem. (2009) 3972–3981.

[19] A.R. Jeong, J.W. Shin, J.H. Jeong, K.H. Bok, C. Kim, D. Jeong, J. Cho, S. Hayami, K.S. Min, Chem. Eur. J. 23 (2017) 3023–3033.

[20] A.R. Jeong, J. Choi, Y. Komatsumaru, S. Hayami, K.S. Min, Inorg. Chem. Commun. 86 (2017) 66–69.

[21] S. Deoghoria, S. Sain, M. Soler, W.T. Wong, G. Christou, S.K. Bera, S.K. Chandra, Polyhedron 22 (2003) 257–262.
[22] S. Sain, S. Bid, A. Usman, H.-K. Fun, G. Aromí, X. Solans, S.K. Chandra, Inorg. Chim. Acta 358 (2005) 3362–3368.
[23] A. Escuer, G. Aromí, Eur. J. Inorg. Chem. 2006, 4721–4736.
[24] F.A. Mautner, B. Sudy, C. Berger, R.C. Fischer, R. Vicente, Polyhedron 42 (2012) 95–101.
[25] A.N. Georgopoulou, C.R. Raptopoulou, V. Psycharis, R. Ballesteros, B. Abarca, A.K. Boudlais, Inorg. Chem. 48 (2009) 3167–3176.
[26] H.-Z. Kou, S. Hishiya, O. Sato, Inorg. Chim. Acta, 361 (2008) 2396–2406.
[27] M.Č. Romanović, M.R. Milenković, A. Pevec, I. Turel, V. Spasojević, S. Grubišić, D. Radanović, K. Anđelković, B. Čobeljić, Polyhedron 139 (2018) 142–147.
[28] G. Jonkers, C. A. de Lange, L. Noodleman, E. J. Baerends, Mol. Phys. 46 (1982) 609–620.
[29] L. Noodleman, J. Chem. Phys. 74 (1981) 5737–5743.
[30] L. Noodleman, E. R. Davidson, Chem. Phys. 109 (1986) 131–143.
[31] L. Noodleman, J.G. Norman, J.H. Osborne, A. Aizman, D.A. Case, J. Am. Chem. Soc. 107 (1985) 3418–3426.
[32] F. Neese, Coord. Chem. Rev. 253 (2009) 526–563.
[33] R. Caballol, O. Castell, F. Illas, I.D.P.R. Moreira, J. P. Malrieu, J. Phys. Chem. A 101 (1997) 7860–7866.
[34] I. Ciofini, C.A. Daul, Coordination Chemistry Reviews. Elsevier March 1, 2003, pp 187–209.
[35] A. Bencini, F. Totti, C.A. Daul, K. Doclo, P. Fantucci, V. Barone, Inorg. Chem. 36 (1997) 5022–5030.
[36] A. Bencini, F. Totti, J. Chem. Theory Comput. 5 (2009) 144–154.
[37] P. Comba, S. Hausberg, B. Martin, J. Phys. Chem. A 113 (2009) 6751–6755.
[38] N.A.G. Bandeira, B.Le. Guennic, J. Phys. Chem. A 116 (2012) 3465–3473.
[39] D.A. Pantazis, Inorganics 7 (2019) 57.
[40] R. Costa, D. Reta, I.D.P.R. Moreira, F. Illas, J. Phys. Chem. A 122 (2018) 3423–3432.
[41] P. Rivero, I.D.P.R. Moreira, F. Illas, G.E. Scuseria, J. Chem. Phys. 129 (2008) 184110.
[42] R. Valero, R. Costa, I. De P.R. Moreira, D.G. Truhlar, F Illas, J. Chem. Phys. 128 (2008) 114103.
[43] T. Schwabe, S. Grimme, J. Phys. Chem. Lett. 1 (2010) 1201–1204.
[44] T. Ziegler, A. Rauk, Theor. Chim. Acta 46 (1977) 1–10.
[45] T. Ziegler, A. Rauk, Inorg. Chem. 18 (1979) 1558–1565.
[46] F.M. Bickelhaupt, E.J. Baerends, Reviews in computational chemistry. Wiley-VCH Verlag, London, (2000) pp 1–86
[47] R.F. Nalewajski, J. Mrozek, G. Mazur, Can. J. Chem. 74 (1996) 1121–1130.

[48] M.P. Mitoraj, A. Michalak, T. Ziegler, J. Chem. Theory. Comput. 5 (2009) 962–975.
[49] Oxford Diffraction, CrysAlis PRO, Oxford Diffraction Ltd., Yarnton (England), 2009.
[50] A. Altomare, G. Cascarano, C. Giacovazzo, A. Guagliardi, J. Appl. Crystallogr. 26 (1993) 343–350.
[51] G.M. Sheldrick, Acta. Crystallogr. A64 (2008) 112–122.
[52] G.A. Bain, J.F. Berry, J. Chem. Educ. 85 (2008) 532–536.
[53] T. Soda, Y. Kitagawa, T. Onishi, Y. Takano, Y. Shigeta, H. Nagao, Y. Yoshioka, K. Yamaguchi, Chem. Phys. Lett. 319 (2000) 223–230.
[54] F. Neese, Rev. Comput. Mol. Sci. 2 (2012) 73–78.
[55] C. van. Wüllen, J. Chem. Phys. 109 (1998) 392–399.
[56] F. Weigend, R. Ahlrichs, Phys. Chem. Chem. Phys. 7 (2005) 3297–3305.
[57] D.A. Pantazis, X.-Y. Chen, C. R. Landis, F. Neese, J. Chem. Theory Comput. 4 (2008) 908–919.
[58] P. Chaudhuri, R. Wagner, S. Khanra, T. Weyhermüller, Dalt. Trans. 41 (2006) 4962–4968.
[59] A.D. Becke, Phys. Rev. A 38 (1988) 3098–3100.
[60] J.P.Perdew, Phys. Rev. B 33 (1986) 8822–8824.
[61] J.P. Perdew, Phys. Rev. B 34 (1986) 7406.
[62] C. Lee, W. Yang, R.G. Parr, Phys. Rev. B 37 (1988) 785–789.
[63] B.G. Johnson, P.M.W. Gill, J.A. Pople, J. Chem. Phys. 98 (1993) 5612.
[64] T.V. Russo, R.L. Martin, P.J. Hay, J. Chem. Phys. 101 (1994) 7729.
[65] N.C. Handy, A.J. Cohen, Mol. Phys. 99 (2001) 403–412.
[66] M. Swart, A.W. Ehlers, K. Lammertsma, Mol. Phys. 102 (2004) 2467–2474.
[67] Y. Zhao, D.G. Truhlar, J. Chem. Phys. 125 (2006) 194101.
[68] Y. Zhao, D.G. Truhlar, Theor. Chem. Acc. 120 (2008) 215–241.
[69] J. Tao, J. Perdew, V. Staroverov, G. Scuseria, Phys. Rev. Lett. 91 (2003) 146401.
[70] V.N. Staroverov, G.E. Scuseria, J. Tao, J.P. Perdew, J. Chem. Phys. 119 (2003) 12129.
[71] A.D. Becke, J. Chem. Phys. 98 (1993) 5648–5652.
[72] M. Reiher, O. Salomon, B. Artur Hess, Theor. Chem. Acc. 107 (2001) 48–55.
[73] S. Grimme, J. Chem. Phys. 124 (2006) 034108.
[74] L. Goerigk, S. Grimme, J. Chem. Theory Comput. 7 (2010) 291–309.
[75] F. Neese, F. Wennmohs, A. Hansen, U. Becker, Chem. Phys. 356 (2009) 98–109.
[76] D.A. Pantazis, F. Neese, Theory Comput. 5 (2009) 2229–2238.
[77] F. Weigend, Phys. 8 (2006) 1057–1065.
[78] F. Neese, J. Chem. Phys. 115 (2001) 11080–11096.
[79] A. Hellweg, C. Hättig, S. Höfener, W. Klopper, Theor. Chem. Acc. 117 (2007) 587–597.

[80] P. Ghorai, P. Brandão, S. Benmansour, C.J.G. García, A. Saha, Polyhedron 188 (2020) 114708.
[81] S. Grimme, J. Antony, S. Ehrlich, H. Krieg, J. Chem. Phys. 132 (2010) 154104.
[82] S. Grimme, S. Ehrlich, L. Goerigk, J. Comput. Chem. 32 (2011) 1456–1465.
[83] E.J. Baerends, T. Ziegler, A.J. Atkins et al, ADF2019, SCM, theoretical chemistry. Vrije Universiteit, Amsterdam. http://www.scm.com
[84] G. te Velde, F.M. Bickelhaupt, E.J. Baerends, C. Fonseca Guerra, S.J.A. van Gisbergen, J.G. Snijders, T. Ziegler, J. Comput. Chem. 22 (2001) 931–967.
[85] C.F. Guerra, J.G. Snijders, G. te Velde, E.J. Baerends, Theor. Chem. Acc. 99 (1998) 391–403.
[86] A. Bérces, R.M. Dickson, L. Fan, H. Jacobsen, D. Swerhone, T. Ziegler, Comput. Phys. Commun. 100 (1997) 247.
[87] H. Jacobsen, A. Bérces, D. Swerhone, T. Ziegler, Comput. Phys. Commun. 100 (1997) 263.
[88] N.W. Ashcroft, N.D. Mermin, Solid State Physics, Saunders College Publishing, USA (1976).
[89] O. Kahn, Molecular Magnetism, VCH Publishing, 1993.
[90] L. Goerigk, S. Grimme, Mol. Sci. 4 (2014) 576–600.
[91] T. Schwabe, S. Grimme, Acc. Chem. Res.41 (2008) 569–579.
[92] L. Goerigk, S. Grimme, Phys. Chem. Chem. Phys. 13 (2011) 6670–6688.
[93] L. Goerigk, A. Hansen, C. Bauer, S. Ehrlich, A. Najibi, S. Grimme, Phys. Chem. Chem. Phys. 19 (2017) 32184–32215.
[94] N. Mardirossian, M. Head-Gordon, Mol. Phys. 115 (2017) 2315–2372.
[95] T. Gupta, T. Rajeshkumar, G. Rajaraman, Phys. Chem. Chem. Phys. 16 (2014) 14568–14577.
[96] K.D. Vogiatzis, W. Klopper, A. Mavrandonakis, K. Fink, Chem. Phys. Chem. 12 (2011) 3307–3319.
[97] F. Neese, J. Phys. Chem. Solids 65 (2004) 781–785.
[98] D.A. Pantazis, V. Krewald, M. Orio, F. Neese, Dalt. Trans. 39 (2010) 4959–4967.
[99] Y. Zhang, W. Yang, J. Chem. Phys. 109 (1998) 2604–2608.
[100] M. Parthey, M. Kaupp, Chem. Soc. Rev. 43 (2014) 5067–5088.

Schemes and Figures captions

Scheme 1. Different azido bridging modes.

Scheme 2. Synthesis of a) ligand **HL**Cl, b) complexes $[Ni_2\mathbf{L}_2(\mu\text{-}_{1,1}\text{-}N_3)_2(N_3)_2]$.

Fig.1. ORTEP presentations of the a) $[Ni_2\mathbf{L}_2(\mu\text{-}_{1,1}\text{-}N_3)_2(N_3)_2]\cdot 2H_2O$ (**1a**) and b) $[Ni_2\mathbf{L}_2(\mu\text{-}_{1,1}\text{-}N_3)_2(N_3)_2]\cdot 4H_2O$ (**1b**). Thermal ellipsoids are drawn at the 30% probability level. Unlabeled part of the dimeric molecules (**1a**) and (**1b**) and the corresponding solvent water molecules are generated by symmetry operations -x+1, -y, -z+1and -x+1, -y, -z, respectively.

Fig. 2. Temperature dependence of susceptibility χ and product $\chi \cdot T$ (inset) of **1** measured in a magnetic field of 1 kOe. The full green line is a fit with function (2) and parameters described in the main text.

Fig. 3. Graphical representation of the spin density of the high-spin state of the binuclear complexes **1a**and **1b**. Isosurfaces were drawn at 0.01 e/Å^3 with blue surfaces representing α-spin.

Fig. 4. Corresponding orbitals obtained from the broken-symmetry solution of the binuclear complexes **1a** and **1b**. α spin-orbitals are depicted as red (positive)/yellow (negative) lobes; β spin-orbitals are depicted as blue (positive)/grey (negative) lobes. Isosurfaces were drawn at 0.04 e/Å^3. Their spatial overlaps are: 0.00026 and 0.00169 (**1a**); 0.00389 and 0.00186 (**1b**),

Fig. 5 Most important density deformation channels from EDA–NOCV analysis of the formation of dimeric structures of **1a** (up) and **1b** (down). Their relevance is given by their energy contribution E_σ to E_{orb}. Charge outflow/inflow is represented by yellow/blue color (isovalue = 0.004 a.u.)